tical to that used in several recent studies of the dissociation of C_{60} and C_{60}^+ (*16*)]. As a test of the model used to estimate the internal energy of the injected clusters, we used this method to determine dissociation energies for some of the smaller carbon clusters and found them to be in reasonable agreement with the values recently reported by Anderson and co-workers (*17*). In Fig. 4B the threshold for appearance of the fullerene fragments (which is nearly identical to the threshold for loss of the polycyclic rings) is compared with the threshold calculated with an activation energy of 2.4 eV. The calculated threshold is significantly sharper than that observed experimentally. Most of this discrepancy probably arises from the presence of a number of different polycyclic ring isomers with slightly different activation energies. From these simulations, we estimate an average activation energy of ~2.4 eV for annealing of the polycyclic rings and ~3.7 eV for annealing the monocyclic ring. These activation energies are sufficiently small that both of these processes may play an important role in the carbon arc synthesis of fullerenes where temperatures have been estimated to be 1000 to 2000 K (*18*). Conversion from the planar polycyclic and monocyclic rings to a closed shell of hexagonal and pentagonal rings must surely represent some of the most dramatic molecular rearrangements in modern chemistry, yet the activation energies for these processes appear to be comparable to the strength of a single C–C bond. The driving force for these structural interconversions is the overwhelming stability of the spheroidal shell, which is clearly demonstrated by the fact that a substantial fraction of the fullerenes generated by annealing of the polycyclic rings are produced sufficiently excited that they subsequently fragment.

We have performed similar studies of other carbon cluster ions containing 50 to 70 atoms and found that the behavior reported here for C_{60}^+ is not unique: for example, annealing of a 58-atom cluster to a spheroidal fullerene occurs almost as easily as for a 60-atom cluster. However, for clusters with fewer than 50 atoms, fullerene formation diminishes sharply as annealing into large monocyclic rings becomes the dominant process. Hence, our studies confirm that coalescence of medium-sized polyyne rings followed by annealing is likely to be an important route in fullerene synthesis. However, while annealing of the polycyclic rings provides a direct route to the large spheroidal fullerenes, this process cannot apparently account for why some specific fullerenes are formed in such large relative abundances (unless the behavior of C_{60} is dramatically different to that of C_{60}^+). After formation of a large spheroidal shell, presumably it is their low reactivity toward small carbon species such as C_2 (6) that is responsible for the preponderance of certain fullerenes. Because formation of a spheroidal fullerene is not unique to C_{60}^+, these results suggest that preparation of a polyyne precursor, followed by photochemical activation in an inert environment, may provide a general route for the synthesis of fullerenes of any size. The challenge now is to determine which of the possible polyyne ring isomers are the best potential precursors.

REFERENCES AND NOTES

1. Q. L. Zhang *et al.*, *J. Phys. Chem.* **90**, 525 (1986); H. Kroto, *Science* **242**, 1139 (1988).
2. T. W. Ebbesen, J. Tabuchi, K. Tanigaki, *Chem. Phys. Lett.* **191**, 336 (1992).
3. A. Goeres and E. Sedlmayr, *ibid.* **184**, 310 (1991); M. Broyer *et al.*, *ibid.* **198**, 128 (1992).
4. T. Wakabayashi and Y. Achiba, *ibid.* **190**, 465 (1992).
5. T.-M. Chang, A. Naim, S. N. Ahmed, G. Goodloe, P. B. Shevlin, *J. Am. Chem. Soc.* **114**, 7603 (1992).
6. J. R. Heath, *ACS Symp. Ser.* **481**, 1 (1991).
7. Y. Rubin, M. Kahr, C. B. Knobler, F. Diederich, C. L. Wilkins, *J. Am. Chem. Soc.* **113**, 495 (1991); S. W. McElvaney, M. M. Ross, N. S. Goroff, F. Diederich, *Science* **259**, 1594 (1993).
8. M. F. Jarrold and V. A. Constant, *Phys. Rev. Lett.* **67**, 2994 (1991); M. F. Jarrold and J. E. Bower, *J. Chem. Phys.* **96**, 9180 (1992).
9. M. F. Jarrold and E. C. Honea, *J. Phys. Chem.* **95**, 9181 (1991); *J. Am. Chem. Soc.* **114**, 459 (1992).
10. G. von Helden, M.-T. Hsu, P. R. Kemper, M. T. Bowers, *J. Chem. Phys.* **95**, 3835 (1991); see also R. M. Baum, *Chem. Eng. News* **70** (no. 22), 25 (1992).
11. J. Hunter, J. Fye, M. F. Jarrold, *J. Phys. Chem.*, in press.
12. E. A. Mason and E. W. McDaniel, *Transport Properties of Ions in Gases* (Wiley, New York, 1988).
13. L. A. Bloomfield, M. E. Geusic, R. R. Freeman, W. L. Brown, *Chem. Phys. Lett.* **121**, 33 (1985); S. C. O'Brien, J. R. Heath, R. F. Curl, R. E. Smalley, *J. Chem. Phys.* **88**, 220 (1988); R. J. Doyle and M. M. Ross, *J. Phys. Chem.* **95**, 4954 (1991).
14. M. E. Geusic, M. F. Jarrold, T. J. McIlrath, R. R. Freeman, W. L. Brown, *J. Chem. Phys.* **86**, 3862 (1987); P. P. Radi, T. L. Bunn, P. R. Kemper, M. E. Molchan, M. T. Bowers, *ibid.* **88**, 2809 (1988).
15. W. Forst, *Theory of Unimolecular Reactions* (Academic, New York, 1973).
16. R. K. Yoo, B. Ruscic, J. Berkowitz, *J. Chem. Phys.* **96**, 911 (1992); P. Wurz and K. R. Lykke, *J. Phys. Chem.* **96**, 10129 (1992); P. Sandler, C. Lifshitz, E. Klots, *Chem. Phys. Lett.* **200**, 445 (1992).
17. M. B. Sowa, P. A. Hintz, S. L. Anderson, *J. Chem. Phys.* **95**, 4719 (1991).
18. R. E. Haufler *et al.*, *Mater. Res. Soc. Symp. Proc.* **206**, 627 (1991).

15 January 1993; accepted 6 April 1993

A Photomicrodynamic System with a Mechanical Resonator Monolithically Integrated with Laser Diodes on Gallium Arsenide

Hiroo Ukita, Yuji Uenishi, Hidenao Tanaka

A cantilever resonant microbeam, laser diodes, and a photodiode have been fabricated on the surface of a gallium arsenide substrate. The microbeam is excited photothermally by light from a laser diode. The vibration is detected with a photodiode as the variation in light output caused by the difference in optical length between the microbeam and another laser diode. A high carrier-to-noise ratio (45 decibels) is achieved with a short (3 micrometers) external cavity length. Such a small distance allows a lensless system, which increases the ease of fabrication. This work could lead to applications in which photomicrodynamic systems are monolithically integrated on a gallium arsenide substrate with surface micromachining technology.

Established large-scale integration manufacturing techniques, such as photolithography, can be used for fabricating microstructures including resonant sensors, motors, valves, and pumps (*1–3*). Such microdevices have been made from silicon wafers, which have isodirectional etching properties. However, it has been impossible to integrate a light source with these Si-based micromechanical structures. Gallium arsenide (GaAs), on the other hand, is attractive for integrating optical and mechanical structures. The advantage of using an optical method is that it does not interfere electromagnetically. Furthermore, it could lead to developments in photomicrodynamics. With GaAs, not only would optical sensors and actuators be possible, but also micromechanical filters for optical signal processing and pickups for optical recording (*4, 5*).

A resonant sensor is a device that changes its mechanical resonant frequency as a function of a physical or chemical parameter, such as stress or mass-loading (*6*). Electrostatic (capacitive) excitation and detection or piezoelectric excitation and detection have been used for the conventional Si-based resonant sensors. The former method requires comparatively large electrode areas and small electrode distances (a few micrometers) if good signals are to be obtained. The latter requires a layer of a

NTT Interdisciplinary Research Laboratories, 9-11 Midori-cho 3-Chome, Musashino-shi, Tokyo 180, Japan.

piezoelectric material, preferably zinc oxide (ZnO). Unfortunately, however, ZnO is not compatible with integrated-circuit technology.

We have fabricated a resonant sensor on the surface of a GaAs substrate (Fig. 1) that uses optical excitation and detection. The cantilever microbeam is shaped by reactive dry-etching and undercut by selective wet-etching (the etching of AlGaAs is inhibited in highly Al-doped regions) so that it is free to vibrate. Light incident from laser diode LD2 on the side wall of the microbeam (MB) will be partially absorbed, heating the MB and producing the bending moment (7). The MB is excited by the thermal stress of the resonant frequency caused by a pulsed laser diode LD2.

This sideways vibration is detected by LD1 and photodiode PD from the variation in the external cavity length between the MB wall and the facet of LD1 (phase difference). The light incident from LD1 is continuous, and the amount of light is so small that it has no effect on the MB vibration. The light (wavelength λ = 830 nm) reflected from the MB wall interferes with the light from the facet of LD1. Maximum peaks in the light output occur every $\lambda/2$, and their amplitude decays exponentially in proportion to the external cavity length (8). The variation in light output caused by this vibration is detected as a signal by the PD.

The resonator was designed to optimize the efficiency of the photothermal excitation and the quality of the composite cavity signal with the structural configuration resulting from the fabrication process. We set the distance h_1 between the facet LD1 and the wall of the MB equal to 3.0 μm by considering the composite cavity signal-to-noise ratio and the aspect ratio h_1/w of the reactive dry-etching process. We set the distance h_2 between the facet of LD2 and the wall of the MB equal to 30 μm on the basis of the energizing light absorption on the MB and the hole size for the wet process described later. For the MB dimensions we used a length ℓ = 50 or 110 μm, a thickness t = 3 μm, and a depth w = 5 μm, considering the resonant frequency of the MB. We determined the positions of the exciting light beam (LD2) and the detecting light beam (LD1) on the MB wall based on the consideration that the LD2 light strikes the MB closer to the support for better excitation and that the LD1 light strikes farther from the support for better detection and also to prevent "cross-talk" between the two light beams.

The short distance of the LD1-MB-LD2 structure is useful for a vibration resonator because no lenses are required in the structure to make the light beam converge, so it is easier to integrate the mechanical element with the optical elements. Furthermore, the integrated structure does not need any optical alignment like that required by conventional hybrid resonant sensors.

Three micromachining processes (Fig. 2) were carried out to fabricate a resonant MB integrated with two laser diodes: (i) An etch-stop layer of AlGaAs was formed in the laser diode structures prepared by metal organic vapor-phase epitaxy (Fig. 2A). (ii) The shape of the microstructure was precisely defined by means of a reactive dry-etching [reactive fast atom beam (9)] technique with chlorine, which can simultaneously form the vertical etched mirror facets for LDs (Fig. 2B). (iii) A wet-etch window was made with photoresist, and the microbeam was undercut by selective etching [sacrificial layer etching (10)] to leave the

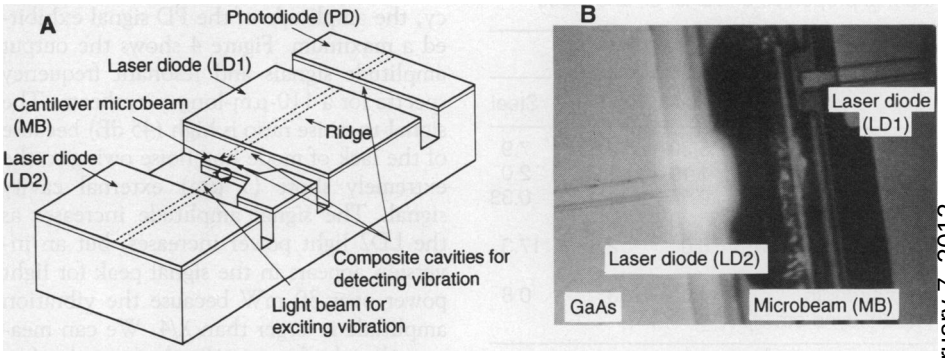

Fig. 1. (**A**) Structure and (**B**) photograph of a resonator sensor driven photothermally from one side (30 μm away) by laser diode LD2 and sensed optically from the other side (3 μm away) by laser diode LD1 and photodiode PD; LD1, LD2, and PD are integrated on a GaAs substrate by surface micromachining techniques.

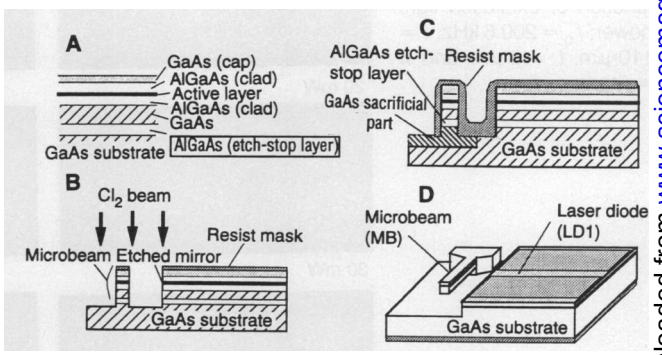

Fig. 2. Process steps used to fabricate a GaAs/AlGaAs resonant microbeam (MB) integrated with a laser diode (LD). (**A**) An AlGaAs etch-stop layer is introduced in the epitaxial growth. (**B**) The mechanical structure is defined by the shape of a mask and dry-etched by reactive fast atom beam etching with chlorine. (**C**) The mechanical structure is released from the GaAs substrate by wet-etching, which removes the sacrificial region. The bottom of the structure is protected by the etch-stop layer. The photoresist used to protect the top surface and side walls of the structure is removed by O_2 plasma etching. (**D**) Final structure of the integrated microbeam and laser diode.

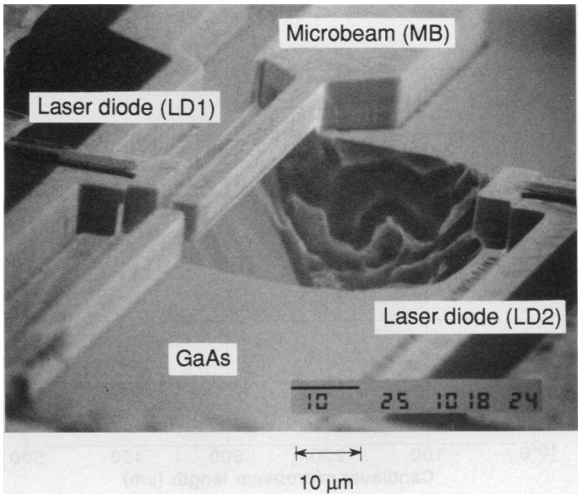

Fig. 3. Scanning electron microscope view of the main parts of the resonant sensor. We fabricated the released GaAs/AlGaAs microbeam (MB) by undercutting the sacrificial GaAs. The MB length, width, and thickness are 110, 3.0, and 5 μm, respectively, and the distances from the facet of LD1 to the side wall of the MB and LD2 to MB are 3.0 and 30 μm, respectively.

microbeam freely suspended (Fig. 2C). The final structure of the integrated microbeam and laser diode is shown in Fig. 2D.

Figure 3 shows a scanning electron microscope image of the main parts of the resonant sensor. The hole for wet-etching is visible under the microbeam between LD1 and LD2. On the basis of the size of the hole, the distance between the MB and LD2 was set to 30 μm. The shorter the MB-LD2 distance, the higher the photothermal conversion efficiency becomes. The threshold current of LD2 was 46 mA and that of LD1 was 64 mA (the threshold current of LD1 is higher because both of its mirrors were etched).

We used a function generator to drive LD2 with a sinusoidal signal to measure the resonant MB properties. When the frequency of the function generator coincided with the MB mechanical resonant frequency, the amplitude of the PD signal exhibited a maximum. Figure 4 shows the output amplitude signals and resonant frequency spectra for a 110-μm-long microbeam. The signal-to-noise ratio is high (45 dB) because of the lack of mode hop noise owing to the extremely short (3 μm) external cavity signal. The signal amplitude increases as the LD2 light power increases, but an inversion appears in the signal peak for light power over 30 mW because the vibration amplitude is larger than λ/4. We can measure the absolute amplitude from the fact that the peak signal amplitude corresponds to λ/4 (0.21 μm). As the incident light power rises, producing greater thermal expansion (stress) in the microbeam, the vibration amplitude increases. The resonances of the microbeam for lengths of 110 and 50 μm are 200.6 kHz and 1.006 MHz, respectively. The mechanical quality (Q) values in air are ~250. If the Q values are to be increased, damping mechanisms such as imbalance and radiation at the supporting rim will require further study.

Table 1. Comparison of the mechanical and thermal properties of GaAs, Si, and steel.

Parameter	Material		
	GaAs	Si	Steel
ρ (g cm^{-2})	5.307	2.3	7.9
E (10^{12} dyne cm^{-2})	1.19	1.9	2.0
Thermal conductivity (W cm^{-1} K^{-1})	0.54	1.57	0.33
Thermal expansion (10^{-6} K)	6.0	2.5	17.3
Yield strength (10^{10} dyne cm^{-2})	4.0*	13*	0.8

*Single crystalline.

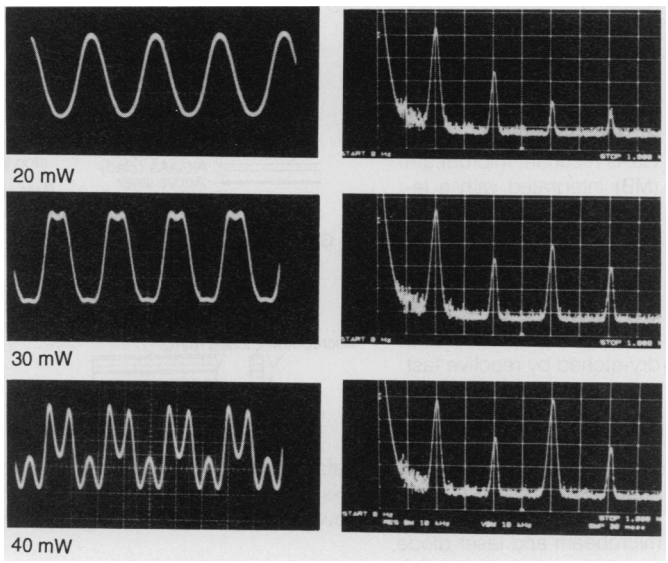

Fig. 4. Variations in MB vibration amplitude and its frequency spectrum as a function of excitation light power; f_0 = 200.6 kHz, ℓ = 110 μm, t = 3 μm, and w = 5 μm.

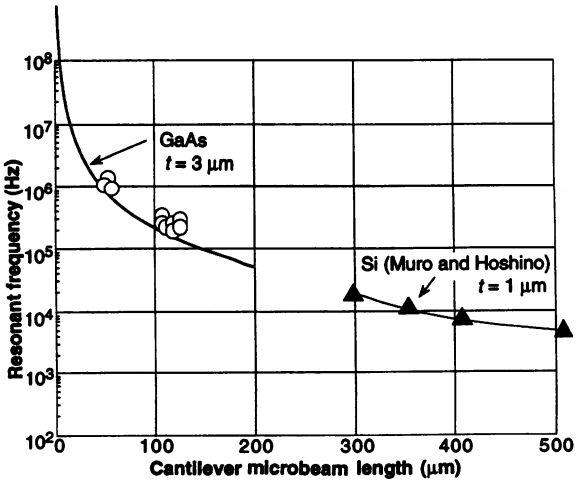

Fig. 5. Resonance frequency as a function of cantilever microbeam length for GaAs and Si. The solid lines are theoretical results; the circles and triangles are experimental measurements for GaAs and Si, respectively (*11*).

Figure 5 shows the resonance frequency as a function of microbeam (cantilever) length for GaAs and Si. The circles and triangles are experimental measurements for GaAs and Si, respectively (*11*), and they are in good agreement with the theoretical results (*12*) calculated from Eq. 1 using the parameter values listed in Table 1

$$f_0 = \lambda_0^2 t(E/12\rho)^{1/2}/2\pi\ell^2 \quad (1)$$

where λ_0 is the eigen value of 1.875 determined by the vibration mode, E is Young's modulus, ρ is the density, ℓ is the cantilever length, and t is its thickness. To increase the sensor sensitivity, the resonant frequency should be raised by shortening the cantilever length. A resonant frequency of 10 MHz is available with a length of less than 20 μm (3 μm thick), if Eq. 1 is valid for a beam of micrometer-scale length. The physical properties of a microstructure usually differ somewhat from bulk values (*13*), but the bulk parameters can indicate relative trends in the micromechanical properties of the materials.

Monolithic structures that integrate a mechanical element, such as a resonant MB, with optical elements, such as an LD and a PD, on a single GaAs substrate promise many applications. These include resonant frequency change-detection sensors such as accelerometers for control systems and mechanical filters that would synchronize signal detection in communication systems. The yield strength of single crystalline GaAs is less than that of Si (see Table 1), but it is five times that of steel. Furthermore, surface micromachining can be used to fabricate microstructures of high purity with a low defect density and no residual stress. These mechanical properties make GaAs-based microstructures suitable for integrated photomicrodynamic systems. This technology could have a significant effect on engineering design and interdisciplinary activity.

REFERENCES AND NOTES

1. K. E. Drexler, *Engines of Creation* (Anchor Books, Doubleday, New York, 1987), p. 3.
2. R. S. Muller, *Sensors Actuators* **A21–23**, 1 (1990).
3. K. D. Wise and K. Najafi, *Science* **254**, 1335 (1991).
4. H. Ukita, Y. Katagiri, S. Fujimori, *Appl. Opt.* **28**, 4360 (1989).

5. J.-Y. Kim and H. C. Hseih, *J. Lightwave Technol.* **10**, 439 (1992).
6. G. Stemme, *J. Micromech. Microeng.* **1**, 113 (1991).
7. K. Hane and S. Hattori, *Appl. Opt.* **29**, 145 (1990).
8. H. Ukita, Y. Katagiri, Y. Uenishi, *Jpn. J. Appl. Phys.* **26** (suppl. 26-4), 111 (1987).
9. F. Shimokawa, H. Tanaka, Y. Uenishi, R. Sawada, *J. Appl. Phys.* **66**, 2613 (1989).
10. Z. L. Zhang, G. A. Porkolab, N. C. MacDonald, in *Proceedings of IEEE Micro Electro Mechanical System '92*, W. Benecke and H.-C. Petzold, Eds. (Travemünde, Germany, 4 to 7 February 1992) (IEEE, New York, 1992), p. 72.
11. H. Muro and S. Hoshino, *Trans. Inst. Electron. Inf. Commun. Eng.* **J74-C-II**, 421 (1991) (in Japanese).
12. M. Tabib-Azar and J. S. Leave, *Sensors Actuators*, **A21–23**, 229 (1990).
13. D. Walsh and B. Culshaw, *ibid.* **A25–27**, 711 (1991).
14. We thank K. Itao and E. S. Vera for helpful discussions.

29 September 1992; accepted 2 February 1993

X-ray Tomographic Study of Chemical Vapor Infiltration Processing of Ceramic Composites

J. H. Kinney, T. M. Breunig, T. L. Starr, D. Haupt, M. C. Nichols, S. R. Stock, M. D. Butts, R. A. Saroyan

The fabrication of improved ceramic-matrix composites will require a better understanding of processing variables and how they control the development of the composite microstructure. Noninvasive, high-resolution methods of x-ray tomography have been used to measure the growth of silicon carbide in a woven Nicalon-fiber composite during chemical vapor infiltration. The high spatial resolution allows one to measure the densification within individual fiber tows and to follow the closure of macroscopic pores in situ. The experiments provide a direct test of a recently proposed model that describes how the surface area available for matrix deposition changes during infiltration. The measurements indicate that this surface area is independent of the fiber architecture and location within the preform and is dominated by large-scale macroporosity during the final stages of composite consolidation. The measured surface areas are in good agreement with the theoretical model.

High fracture toughness and strength give ceramic-matrix composites an advantage over monolithic ceramics. Ceramic-matrix composites, particularly those based on silicon carbide (SiC), can withstand high temperatures and corrosive environments. Accordingly, their use is beginning to be considered necessary in advanced aircraft engine structures and heat management applications. Before these materials can fulfill their potential, however, their fabrication costs must be reduced greatly and their mechanical properties must be improved. Improvements in mechanical properties will come about largely through reduced and controlled residual porosity, which will require better understanding of processing variables and how they ultimately relate to the composite microstructure.

Chemical vapor infiltration (CVI) is an important technology for the fabrication of SiC ceramic-matrix composites (*1*). In CVI, a vapor precursor of the matrix material, methyltrichlorosilane (MTS), is passed through a network of reinforcing fibers at elevated temperature. The MTS dissociates, and the SiC matrix phase deposits on the fibers. As matrix growth progresses, avenues for gas transport become more constricted and begin to close off, eventually stopping the infiltration process. Pore closure determines the final density of the composite.

The manufacture of woven-fiber, ceramic-matrix composites is, in some ways, similar to the technology of textile weaving. Thin (diameters of 10 to 20 μm) fibers are combined into bundles (tows) and are woven into cloth. The cloth layers are formed into a nearly final shape called a preform, which is then infiltrated with MTS. The architecture of the cloth (that is, the geometry of the weave) can be as simple as a square, two-dimensional weave or as complicated as a three-dimensional (3D) weave. In the lay-up of the cloth, the tow directions may be identical between layers (a 0°/90° architecture) or they may be rotated between layers (for example, a 0°/45° or 0°/30°/60° architecture). The architecture determines the directionality of the mechanical properties and may affect the infiltration behavior.

In the woven structure are two distinct classes of porosity. The voids within the fiber tows are called micropores, and the separations between cloth layers (channels) and the interstices that form between the intersecting tows in the cloth (holes) are called macropores. The channels and holes are the primary avenues for vapor transport through the preform; hence, infiltration-induced changes in the macropore dimensions will greatly affect vapor flow and composite consolidation.

In addition to the effects of the macropores on vapor flow, the rate at which the matrix phase grows is strongly influenced by the reaction rates and by the amount of surface area available for deposition. The reaction rates for MTS decomposition and SiC growth have been reported (*2*). The surface area, however, depends on the microstructure of the composite. Because of the small surface areas of both micro- and macropores ($<<500$ cm^2 g^{-1}), independent measurements of the surface area during infiltration cannot be made with traditional techniques such as Brunauer, Emmett, Teller gas adsorption or Hg porosimetry, which both require larger surface areas (*3*). Prior attempts at metallurgical sectioning and stereological measurements have been inconclusive, primarily because the small number of pores, coupled with strong anisotropy, requires an inordinate number of sections to obtain good statistics (*4*).

A model of surface area (the uniform deposition model) has recently been proposed to describe the CVI process in the woven architecture of continuous fiber composites (*5*). This model assumes that the fiber tows occupy 70% of the total volume and that they are ~40% porous [the remaining space is occupied by channel porosity (25%) and hole porosity (5%)]. Before infiltration, the majority of the available surface area is within the tows. As infiltration proceeds, the small pores within the tows fill in rapidly, and the surface area decreases dramatically. When the composite reaches a fractional density of ~70%, the surface area becomes dominated by the macropores, which, because of their larger size, fill in more slowly. The last 30% of consolidation is financially costly because most of the infiltration time is expended during this phase.

To test the validity of the uniform deposition model and to quantify the changes in surface area occurring during infiltration, we have used a noninvasive volume-imaging technique to analyze the microstructure and macrostructure of a woven-fiber composite. Carlson and Denison demonstrated that x-ray microtomography is an effective technique for providing statistically valid microstructural information when conventional sectioning fails to do so (*6*). However, the spatial resolution of the industrial microtomography system (150 μm) used in their experiment is not adequate to provide accurate measurements of the surface area of continuous fiber composites.

New approaches to high-resolution x-ray tomography with solid-state detectors and monochromatic synchrotron radiation pro-

J. H. Kinney, D. Haupt, R. A. Saroyan, Lawrence Livermore National Laboratory, Livermore, CA 94551.
T. M. Breunig and M. C. Nichols, Sandia National Laboratories, Livermore, CA 94550.
T. L. Starr, S. R. Stock, M. D. Butts, Georgia Institute of Technology, Atlanta, GA 30332.